Predicting ballistic impact failure of aluminium 6061-T6 with the rate-independent Bao–Wierzbicki fracture model

A. Gilioli [a], A. Manes [a,*], M. Giglio [a], T. Wierzbicki [b]

[a] Politecnico di Milano, Dipartimento di Meccanica, Via la Masa 1, 20156 Milano, Italy
[b] Impact & Crashworthiness Lab, Massachusetts Institute of Technology, 77 Massachusetts Ave, Cambridge, MA 02139, USA

Received 7 March 2014
Received in revised form
9 October 2014
Accepted 12 October 2014
Available online 22 October 2014

1. Introduction

Nowadays safety, reliability and performance in extreme conditions are main issues addressed in the design and assessment of a structure, especially by the aerospace industry. Experimental tests of failure, impact, explosions etc … are very expensive and difficult to carry out but are often required to assess damage tolerance capability of critical structures. Numerical analyses can be effective tools that allow reducing experimental test efforts \ costs \ uncertainties. With this in mind, a reliable numerical description of the material mechanical behaviour, and in particular an accurate model regarding the damage stage, is needed. There is a large literature on plasticity and fracture of metallic materials. For an excellent review of the historical development, as well as comparisons of constitutive models, the reader is referred to [1–3].

In the present paper, the numerical simulations are based on an uncoupled approach between plasticity and fracture. The quadratic Von Mises yield condition is assumed along with the effect of strain rate sensitivity and thermal softening. Therefore, the Johnson–Cook (JC) [4] plasticity formulation is suitable for this purpose. The hardening parameters are determined by averaging the load–displacement response of the tests using an inverse method. The aluminium strain rate parameters in the JC model was taken from a previous publication of the same authors [5]. The thermal softening exponent in the JC model was taken from literature [6]. In the present paper, the bullet is considered as a deformable rather than a rigid body. The bullet is composed of a lead core and a brass jacket. The plasticity calibration of the bullet has been described in previous publications of the authors [7,8] and those data are applied in current work. Because of the complexity of the problem, a constant fracture strain criterion was used to predict the possible fracture and fragmentation of the bullet.

Effort was put in the paper on the study of the multiaxial plasticity and fracture test of specimens made of Al6061-T6. Tests for plane stress specimen have been already reported in the literature in Ref. [9]. In the present paper axisymmetric un-notched and notched specimens are used in conjunction with an MTS multiaxial testing machine available at the Politecnico of Milano covering a wide range of Lode angle and triaxiality parameters. A similar procedure can be seen for a titanium alloy in Ref. [10] and more recently in Ref. [11].

In terms of fracture models two failure criteria have been most recently and successfully used in the literature to describe ballistic performance. One is the Cockcroft-Latham model [12], utilized

* Corresponding author.
E-mail addresses: andrea.gilioli@polimi.it (A. Gilioli), andrea.manes@polimi.it (A. Manes), marco.giglio@polimi.it (M. Giglio), wierz@MIT.EDU (T. Wierzbicki).

Nomenclature

ε_{pl}	plastic strain
η	stress triaxiality
$\overline{\vartheta}$	Lode angle parameter
η_{av}	average stress triaxiality
$\dot{\varepsilon}_{pl}$	strain rate
$\dot{\varepsilon}_0$	reference strain rate
ε_f	strain at failure
A_{JC}	material elastic limit
B_{JC}, n_{JC}	parameters describing the flow stress in JC formulation
m	parameter taking the temperature effect in JC formulations into account
C_{JC}	parameter taking the strain rate effect in JC formulations into account
T	temperature
T_a	room temperature
T_f	melting temperature
σ_h	hydrostatic stress
σ_{VM}	Von Mises stress
D	damage parameter
ξ	normalized third stress invariant
q	second stress invariant
r	third stress invariant
τ	Shear stress
σ_n	normal stress
C_1, C_2, C_3	modified Mohr Coulomb fracture criterion parameter

extensively by the team of Professor Borvik at NTNU [13,14]. Another one, which is actually adopted in the present paper is the Modified Mohr-Coulomb model (MMC), formulated in its most general form in Ref. [15]. In case of ballistic scenarios the MMC is often simplify assuming a plane stress condition. In this case, the MMC is reduced to the Bao-Wierzbicki empirical model (BW), which was shown to provide good description of ballistic performance of single and multi-layer targets [16,17].

All the experimental test, both concerning calibration and impact, have been numerically reproduced adopting the commercial FEM software ABAQUS in an Explicit framework. Solid elements with a reduce integration scheme and a damage removal algorithm have been adopted.

The present paper is divided into six sections. In Section 2, the computational material models are briefly presented. Section 3 deals with the experimental programme of the tests conducted on an uni and multiaxial test machine in quasi-static conditions and at room temperature. Section 4 gives a description of the adopted numerical framework focusing on the calibration of the BW and MMC fracture criteria by the inverse method. The effect of the mesh size was also discussed. Calibrations (tests and numerical models) are carried out using specimen cut from bulk Al6061-T6 material enabling the performance of tests over a wide range of triaxiality/Lode angle. Thus, in Section 5 the capability of the calibrated BW fracture is evaluated on thin specimens; some of these specimens were cut directly from a thin walled tube (identical to the tube adopted for the ballistic test) in order to asses transferability of the parameter performance from bulk to thin specimens.

The final validation is reported in Section 6, in which a ballistic impact test is numerically reproduced. Comparisons between the FE model and the experiment results are presented in terms of the residual velocity of the bullet and the damage shape.

2. Computational material model

2.1. The material constitutive law: Johnson–Cook

The Johnson–Cook (JC) law is a versatile constitutive empiric law where the effect of the strain rate and the temperature are uncoupled. The complete equation of the JC constitutive law is Eq. (1):

$$\sigma = \left[A_{JC} + B_{JC}\left(\varepsilon_{pl}\right)^{n_{JC}}\right]\left[1 + C_{JC}\ln\left(\frac{\dot{\varepsilon}_{pl}}{\dot{\varepsilon}_0}\right)\right]\left[1 - \left(\frac{T - T_a}{T_f - T_a}\right)^{m}\right] \tag{1}$$

Specific values for the parameters regarding temperature and strain rate of 6061-T6 were reported in the literature [18,6,19]. However, recently a complete description of the strain rate sensitivity of Al6061-T6 has been carried out using a Hopkinson bar testing system [5] and these strain rate parameters have been used for the simulation of ballistic impact in present paper.

2.2. Damage ductile criterion

Ductile phenomenological criteria are able to describe the failure phenomena by means of mathematical formulations but are not aimed at providing any physical explanation. In general terms, they are based on the definition of a scalar damage parameter D, Eq. (2):

$$D = \int_0^{\overline{\varepsilon_f}} \frac{\mathrm{d}\varepsilon_{pl}}{\varepsilon_f\left(\eta,\ \overline{\vartheta},\ \dot{\varepsilon}_{pl},\ T\right)} \tag{2}$$

The parameter D is defined as the accumulation of the plastic strain increments $\mathrm{d}\varepsilon_{pl}$ weighted by a function called fracture locus ε_f. The two most influencing parameters on the fracture locus are the stress triaxiality η and Lode angle parameter $\overline{\vartheta}$. The stress triaxiality is a non-dimensional quantity, which accounts for the pressure effect on fracture and is defined in Eq. (3):

$$\eta = \frac{\sigma_h}{\sigma_{VM}} \tag{3}$$

where σ_h is the hydrostatic stress and σ_{VM} is Von Mises equivalent stress. Taking also the Lode angle $\overline{\vartheta}$ into account, leads to a definition of a fracture locus, which is no longer a simple curve (BW) but rather a surface in the 3D space described by triaxiality and Lode angle parameter (MMC). The Lode angle is related to the third deviatoric stress invariant and it describes the relationship between the intermediate principal stress and the minor and major principal stresses. The elements removal algorithm implemented in FE software is based on the evaluation of the D parameter. When it reaches unity, failure is assumed to take place. The damaged element completely loses its stiffness and is suddenly eliminated from the analysis. Consequently, it is evident that damage is not coupled with the constitutive behaviour.

2.2.1. Bao–Wierzbicki fracture locus

The BW's model [1] is an important evolution of the JC [4] one Indeed the JC fracture model is not very accurate especially for the negative triaxiality region and also for high positive triaxialities, so

in Refs. [1,3] Bao and Wierzbicki (BW) developed a more flexible and accurate fracture locus. The BW fracture locus has not a fixed equation but it is based on the empirical fitting of data, hence, scholars have freedom to adopt the most proper interpolating equation according to certain criteria and needs.

The general shape of the fracture locus curve, and in particular for low triaxialities, is at present, a matter of investigation and discussion in the literature and hence much attention has been paid in this work to the range of low triaxiality. Different shapes of the fracture locus for a triaxiality range around zero have been reported in the literature. In particular Clausing [20], Mc Clintock [21] and Viganò [10,22] found a lower strain at failure in a torsion test ($\eta = 0$) than in a tensile test ($\eta = 0.4$) for various metals. Also in this present work, the strain at failure, evaluated with a torsion test, was found to be a local minimum for the fracture locus. Different conclusions have been drawn in Ref. [23] where ferritic steel, carbon manganese steel vanadium and 99.9% pure copper do not to exhibit a minimum in the fracture locus for zero triaxiality.

2.2.2. Modified Mohr–Coulomb fracture locus

Even if the BW fracture locus is more versatile than the simple JC one, it still does not consider the Lode angle effect. Interesting re-sults of bi-axial fracture tests on tubular specimens in the tension/torsion loading frame were published in Ref. [24] and in Refs. [11], while in Ref. [25] the fracture behaviour of Al 6260-T4 aluminium tubes subjected to internal pressure and axial tension, or compression, was studied. These studies clarified that the Lode angle plays a key role in the ductile fracture of metals. The MMC criterion can take this effect into account. The original MC (Mohr-Coulomb) criterion has been largely exploited in rock and soil mechanics [26,27]. Only recently in Refs. [28], the relevance of the two parameters, triaxiality and Lode angle, has been underlined as important even for the ductile fracture of metals. The MMC is a modification of the original criterion whose description and derivation can be found in Ref. [15]. The original MC criterion states that fracture happens when the combination of normal stress, σ_n and shear stress,τ, reaches a critical value on a fracture plane, see Eq. (4)

$$(\tau + C_1\sigma_n) = C_2 \tag{4}$$

C_1 and C_2 are material constants. Historically, C_1 is called the "friction coefficient" and C_2 the "shear resistance". Their value is strictly positive for C_2 ($C_2 > 0$) instead it can be positive or equal to zero for C_1 ($C_1 \geq 0$). In case $C_1 = 0$ the criterion is reduced to the maximal shear stress. The Lode angle parameter is defined as Eq. (5)

$$\overline{\vartheta} = 1 - \arccos\frac{\xi}{\pi} \tag{5}$$

where ζ is the normalized third stress invariant which is calculated as Eq. (6)

$$\xi = \left(\frac{r}{q}\right)^3 \tag{6}$$

where r is the third invariant and q is the second one. After the transformation of Eq. (4) into the space of stress invariants $\overline{\vartheta}$ and ξ, the final form of the MMC fracture locus is Eq. (7)

$$\varepsilon_f = \left(\frac{A}{C_2}\quad C_3 + \frac{\sqrt{3}}{2-\sqrt{3}}(1-C_3)\left(\sec\left(\frac{\overline{\vartheta}\pi}{6}\right) - 1\right)\right) \times \left(\sqrt{\frac{1+C_1^2}{3}}\cos\left(\frac{\overline{\vartheta}\pi}{6}\right) + C_1\left(\eta + \frac{1}{3}\sin\left(\frac{\overline{\vartheta}\pi}{6}\right)\right)\right)^{-\frac{1}{n}} \tag{7}$$

Eq. (7) is valid for power type hardening materials. The values of the parameters C_1, C_2, and C_3, have to be obtained from the calibration procedure. A detailed parametric study was performed by Bai and Wierzbicki in Refs. [28], showing the effects of the parameters C_1, C_2, and C_3 on the fracture locus. The authors demonstrated that C_1 and C_3 control the shape of the fracture locus, whilst C_2 controls its size. In particular according with [29], C_3 is related with the Lode angle dependence: high C_3 values mean there is a high dependence of Lode angle parameter on the fracture locus.

For the plane stress ($\sigma_3 = 0$) a unique relation between triaxiality and Lode angle can be found. Thus, following the approach described in Ref. [9], it is possible to define Eq. (8)

$$-\frac{27}{2}\eta\left(\eta^2 - \frac{1}{3}\right) = \cos(3\vartheta) = \sin\left(\frac{\pi\overline{\vartheta}}{2}\right) \tag{8}$$

The MMC criterion is very effective in the failure prediction for general full 3D load cases but in case of a plane stress scenario, the BW model can be still adopted, obtaining satisfactory results [1,30]. Indeed the BW model, even if it has been historically developed as empirical, later on it has been pointed out [15,31] that the intersection of the 3d fracture locus by s_3 plane produces a similar curve. Another reason why the MMC has not been applied for the ballistic application is due to a lack of the actual subroutine, which at the moment cannot take the strain rate effect on the constitutive law into account. Very recently, Roth and Mohr have done a very important step toward the solution of this issue in Ref. [32]. The authors performed low, intermediate and high strain rate tension tests on flat specimens investigating the effect of strain rate. They found out that for two different steels, the ductility increase significantly (+60%) where the test speed increased from quasi-static up to 4.2 m/s (around 10^3 s^{-1}). Besides the authors numerically reproduced the tests adopting an empirical extension of the Hosford-Coulomb model taking into account the strain rate effect on fracture initiation.

3. Experiments

Al 6061-T6 belongs to the aluminium series 6000 with silicon and magnesium as the principal alloying components. These alloys are formed by heat treatment (in the present case T6) and they show good formability, workability, weldability and shaving. The chemical composition of Al 6061-T6 is described in Table 1, whereas Table 2 summarizes the main physical-chemical properties of Al 6061-T6 [33,34].

T6 stands for a two phases heat treatment. The entire process is based on the precipitation-hardening phenomenon, which results in a large increment in strength with only a minimal reduction of the break elongation.

In order to calibrate a fracture locus over a wide range of triaxiality and Lode angle, several types tests are needed. In addition to the uni-axial tests reported in the literature [1,2,35], also multi axial tests have been carried out. In detail, uniaxial tensile tests have been performed with three different kinds of specimens: one round smooth and two differently notched round specimens, Fig. 1a–c. Two different kinds of multiaxial tests have been performed: pure torsion and mixed tests (torsion plus tension, torsion plus compression), Fig. 1d. Some upsetting tests with cylindrical specimen with different height to diameter ratios (h/D) have been

Table 1
Chemical composition of Al 6061-T6 [33,34].

Al [%]	Mg [%]	Si [%]	Fe [%]	Cu [%]	Mn [%]	Cr [%]	Zn [%]	Ti [%]
98	0.8–1.2	0.4–0.8	0.7	0.15–0.4	0.15	0.04–0.35	0.25	0.15

Table 2
Physical–chemical properties of Al 6061-T6 [33,34].

Volumic mass	2700 [Kg/m^3]
Specific heat	0.89 [J/KgK]
Sound velocity	5350 [m/s]
Elastic modulus	70,000 [MPa]
Shear modulus	26,000 [MPa]
Poisson's coefficient	0.33

also analysed, Fig. 1e. All specimens have been machined from the same bulk Al 6061-T6 thick aluminium alloy plate. Bulk specimen have been chosen in order to make possible practically tests on the multiaxial loading of round specimen.

Each test has been repeated at least twice to confirm the consistency of the values obtained. However, in the following figures only one experimental curve is reported for each type of tests. A summary of the experimental programme is given in Table 3. All the tests have been performed at room temperature and with a

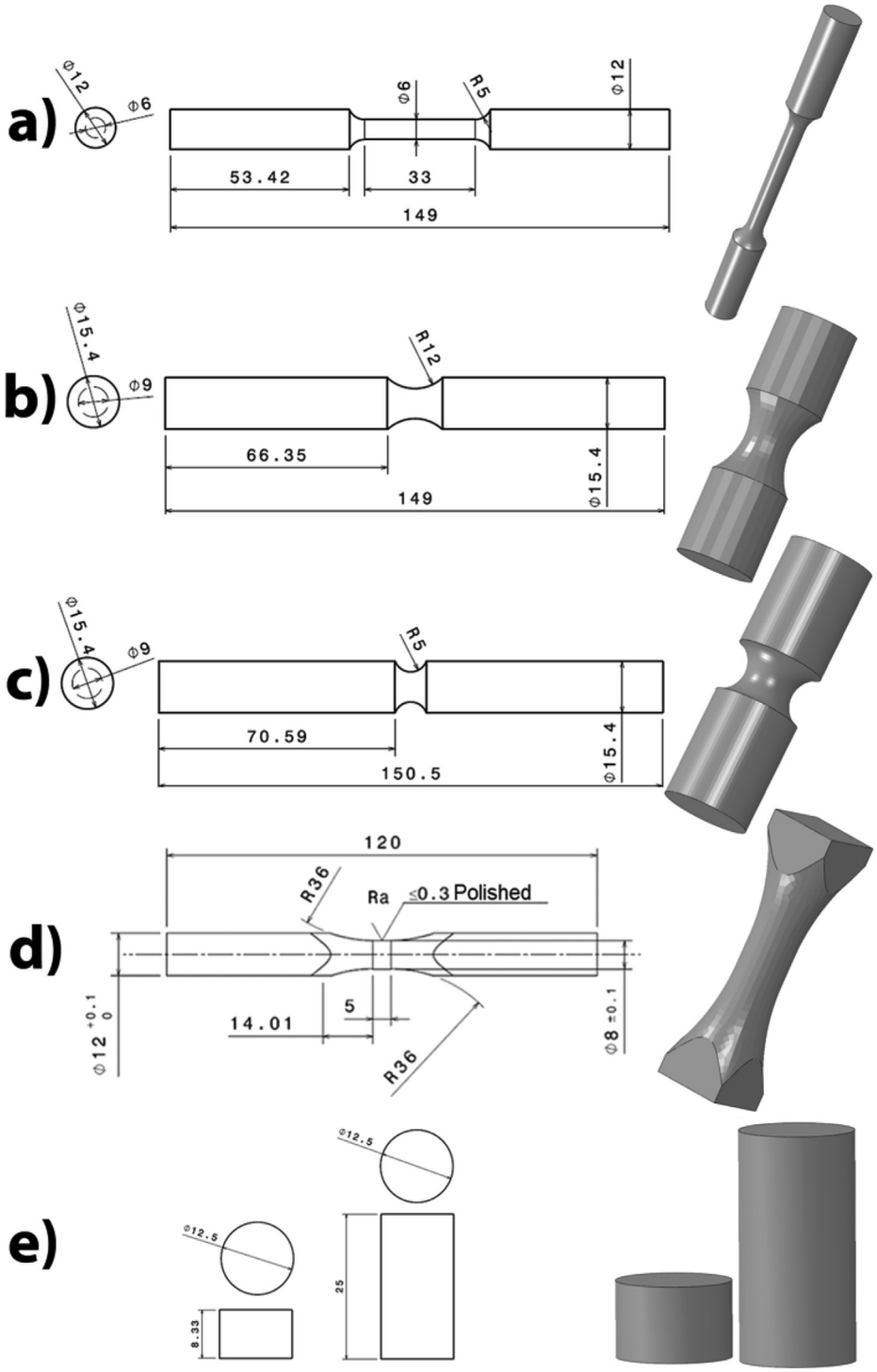

Fig. 1. a) Round smooth specimen, b) Round notched specimen (Notch radius 12 mm), c) Round notched specimen (Notch radius 5 mm), d) Pure torsion and multiaxial specimen, e) Upsetting specimens.

Table 3
Test matrix.

Load case	Load type	Specimen type	Superimposed constant load
Uniaxial	Tension	Round smooth, Fig. 1a	–
Uniaxial	Tension	Round notched. Radius 12 mm, Fig. 1b	–
Uniaxial	Tension	Round notched. Radius 5 mm, Fig. 1c	–
Multiaxial	Torsion	Round smooth, Fig. 1d	–
Multiaxial	Torsion + Tension	Round smooth, Fig. 1d	Tension (4KN)
Multiaxial	Torsion + Tension	Round smooth, Fig. 1d	Tension (8KN)
Multiaxial	Torsion + Compression	Round smooth, Fig. 1d	Compression (12KN)
Uniaxial	Compression	Cylinder, Fig. 1e	–

quasi-static approach: the crosshead velocity was 0.016 mm/s (1 mm/min) for the tensile tests and the rotation speed 1°/s for the torsion and multiaxial tests.

3.1. Experimental test apparatus

Uniaxial tensile tests have been performed using an electro-mechanical MTS Alliance RF150 test system. The load data have been collected from a 150 KN load cell and the displacements have been acquired with an extensometer with a gauge length of 25 mm. A servo hydraulic multi axial machine MTS 809 has been used for the multiaxial tests. The axial load has been acquired with a 250 KN load cell, while a 2200 KN m load cell has been used to measure the torque. The angular rotation has been acquired by the clamp heads of the machine. The multiaxial tests have been carried out in two steps. Firstly by the application of a constant longitudinal load (tension or compression) and then, by imposing a rotation with a fixed rotational velocity until specimen failure is reached.

3.2. Uniaxial tests for high stress triaxialities ($\eta > 0.4$)

In all the uniaxial test an evident "necking phase" is reached before fracture. In the necking area, an inner crack started and quickly propagated causing the failure of the specimen with a sudden fall of the load in the force–displacement curves. Fig. 5 shows various specimen at the end of the experiments. Failure started at the centre of the necked section hence inside the specimen.

3.3. Multiaxial tests for low stress triaxiality ($0 \leq \eta \leq 0.4$)

In order to investigate the low stress triaxiality zone, tests with a multi axial approach (a combination of torsion and longitudinal,

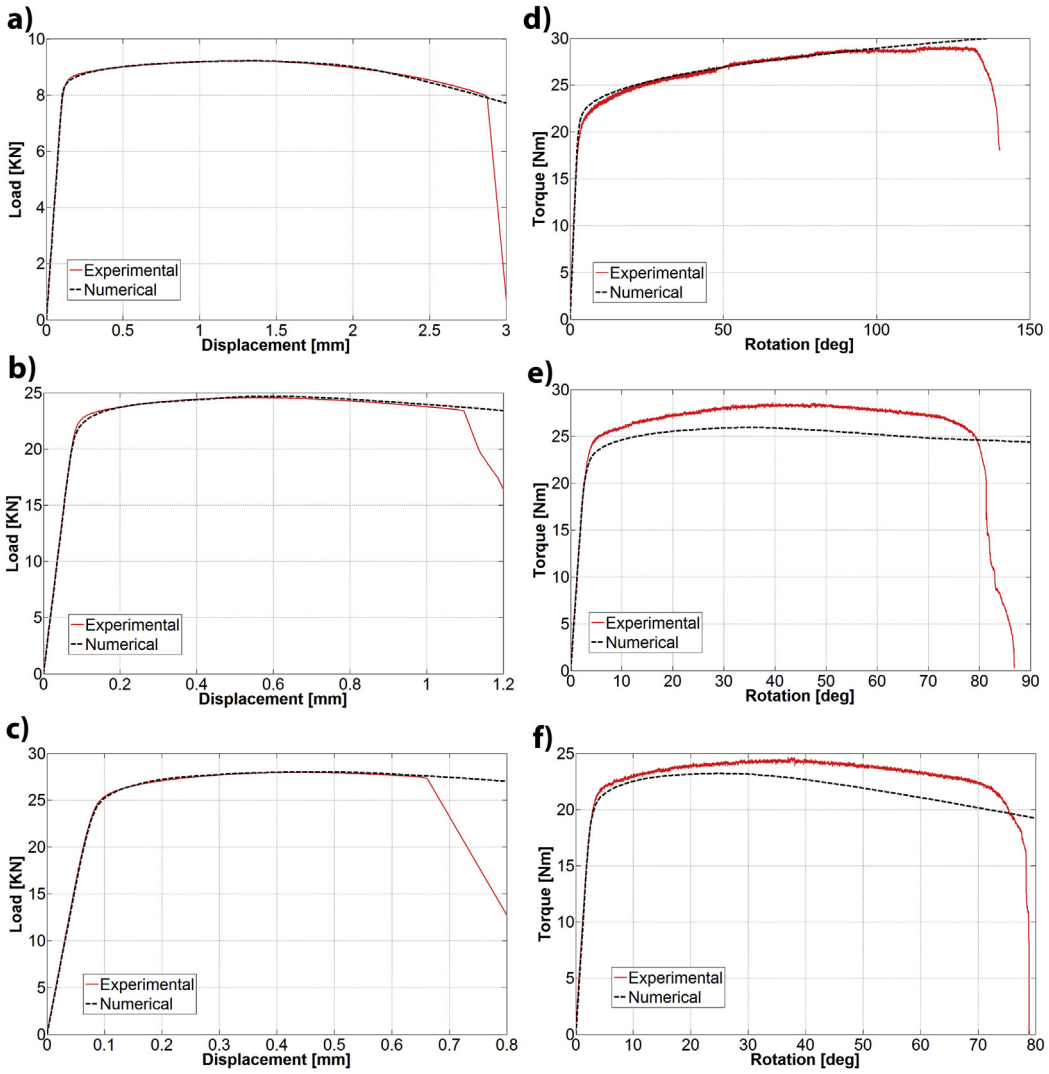

Fig. 2. Comparison between numerical and experimental load–displacement/torque–rotation curves for a) round smooth, b) round notched (notch radius 12 mm), c) round notched (notch radius 5 mm), d) pure torsion test, e) multiaxial (superimposed tension 4KN), f) multiaxial (superimposed tension 8KN).

tension or compression, load) have been carried out with a procedure similar to the one used by Viganò [22]. Commonly in literature, the fracture locus is just extrapolated for stress triaxialities lower than about 0.3–0.4. For example Johnson and Cook in Ref. [4] carried out some pure torsion tests but data from these low triaxiality tests were ignored. During the pure torsion and torsion/compression tests, no necking phenomena were observed. By contrast, during the torsion-tension test necking was visible. The failure mode was not abrupt: the decrease of the load was noticeably smooth. The experimental results showed that the critical rotational value (the critical angle at which the drop of the torque–rotation curve happens) decreased with the increase of the tension load (from 4KN to 8KN). Whereas with a super imposed compression load the rotation to failure rose to very high values. Indeed, it was impossible to reach fracture in the torsion-compression test, despite a rotation of 270°.

3.4. Uniaxial upsetting tests

Several upsetting tests on cylindrical specimens with different height to diameter ratios have been carried out to further assess the previously acquired experimental data. These experimental tests showed that no fracture appears for a pure compression load case. If crack formation occurs, it is located in the equatorial region on the outer surface of the specimens and is caused by not completely avoidable barrelling effects. This scenario has also been reported in the literature in Ref. [36] and the specimens tested in present work show similar behaviour. No further numerical analyses have been performed on these tests.

4. FE analyses

The numerical models have been built with the commercial finite element code ABAQUS V6.11. All the analyses of the test program have been carried out with an Explicit code, using a quasi-static approach, due to the high nonlinear behaviour of the ductile fracture. Solid type elements, with eight nodes and a reduced integration scheme (C3D8R), have been adopted for the mesh. The strain rate and the thermal dependency on plasticity has not been considered in the quasi-static simulations.

An average constitutive law has been obtained using a mean square approach among the optimized laws for the different loading conditions. The final plastic constitutive law obtained for Al 6061-T6 has the following parameters: A_{JC} (270 MPa), B_{JC} (154.3 MPa), n_{JC} (0.2215). These parameters have been re-applied to all "virtual test" models. Fig. 2 shows the comparison between the load–displacement curves obtained experimentally with the curves obtained by the use of the corresponding optimized constitutive law.

4.1. Mesh size effect

Mesh size can strongly affect numerical results and thus its effect has been evaluated. It is important to underline that in order to obtain satisfactory and reasonable results, the numerical models have to fit not only the experimental load⧹displacement curve but, furthermore, they have to be able to reproduce accurately the local stress⧹strain field up to the onset of fracture. The direct consequence is that a simple comparison between the numerical and experimental load⧹displacement curve is not sufficient to assess the capability of the model to reproduce the real phenomenon: the evaluation of the possible local effect of the different mesh size locally is essential. In order to investigate this aspect, also the evolution of the equivalent plastic strain as a function of displacement (rotation) for the most deformed element has been studied, as shown in Fig. 3. The black-hatched area represents an interval of ±10% with respect to the fracture point adopted for the calibration (displacement and rotation), in order to take some experimental variability into account. The value of 10% is merely an indication to help the reader to understand the different weight between mesh size effect and the choice of different displacement⧹rotation at failure. The choice of a 10% variation corresponds at the variability described by the ratio between 0.5 standard deviation over the average value obtained from the tests. It is clear that the severity of the mesh size issue is not identical for each case but depends on the type of load and geometry evaluated. Changing the mesh size has no effect on the plastic strain evolution in the tensile test on a round smooth specimen, see Fig. 3a), but slightly influences the tensile test on the notched specimen, see Fig. 3b). The pure torsion tests and especially the multiaxial (torsion + tension) tests are much more prone to the mesh size effect and Fig. 4 shows the mesh size effect on load/displacement (torque/rotation). The load/displace-ment curve for every kind of specimen is however mainly unaf-fected by the mesh size. It can thus be concluded, that in order to apply an inverse method aimed to study the stress/strain field up to the onset of failure, a good match between the load/displacement curve and the experimental data is not sufficient. In fact, similarity between the two methods is not a guarantee of convergence in the estimation of the local behaviour of the material, especially close to the onset of the fracture.

4.2. Calibration of the BW fracture locus

A correctly calibrated flow stress allows tracking the development of the stress and strain in the critical sites until the onset of fracture.

The approach followed in this work is similar to the one used by Bao and Wierzbicki [1] and Bao [36] meaning that each numerical test can be summarized as a point inside the fracture locus plane. Each point is obtained using the average stress triaxiality, η_{av}, and the equivalent plastic strain (PEEQ) at the onset of the failure, ε_f. The PEEQ is evaluated for the element with the highest strain at the load step when the experimental data show the onset of failure. The average stress triaxiality η_{av} has been calculated following Bao's approach [30] as Eq. (9):

$$\eta_{av} = \frac{1}{\varepsilon_f}\int_0^{\overline{\varepsilon_f}} \eta \mathrm{d}\varepsilon_{pl} \tag{9}$$

Once all the points are collected, the fracture locus can be built by fitting the data. In the present research, the points have been interpolated using the equation of a hyperbola (see Table 4).

As far as negative stress triaxiality is concerned, no fracture was observed in the upsetting tests. This is consistent with the fracture locus curve with a vertical asymptotic value for a stress triaxiality of −1/3 (cut-off value) [36]. Thus, the fracture locus has been built with a hyperbolic equation under the constraint to be asymptotic for a stress triaxiality of −1/3. In Table 4, the fracture locus equation and its calibration are summarized.

A summary of the entire test/simulation programme is shown in Fig. 6. This figure reports the evolution of the plastic strain ε_{pl} versus η, obtained from each numerical simulation of the experi-mental tests. Furthermore, the final average stress triaxiality, η_{av}, and the equivalent plastic strain at the onset of the failure, ε_f, are reported for each test. In Fig. 6, also a comparison between the new BW fracture locus, calibrated in present paper, and a JC fracture locus reported in the literature [6], is presented; clear differences are evident in the negative triaxiality zone and also in high positive triaxiality zone. Calibration points around low triaxiality (between

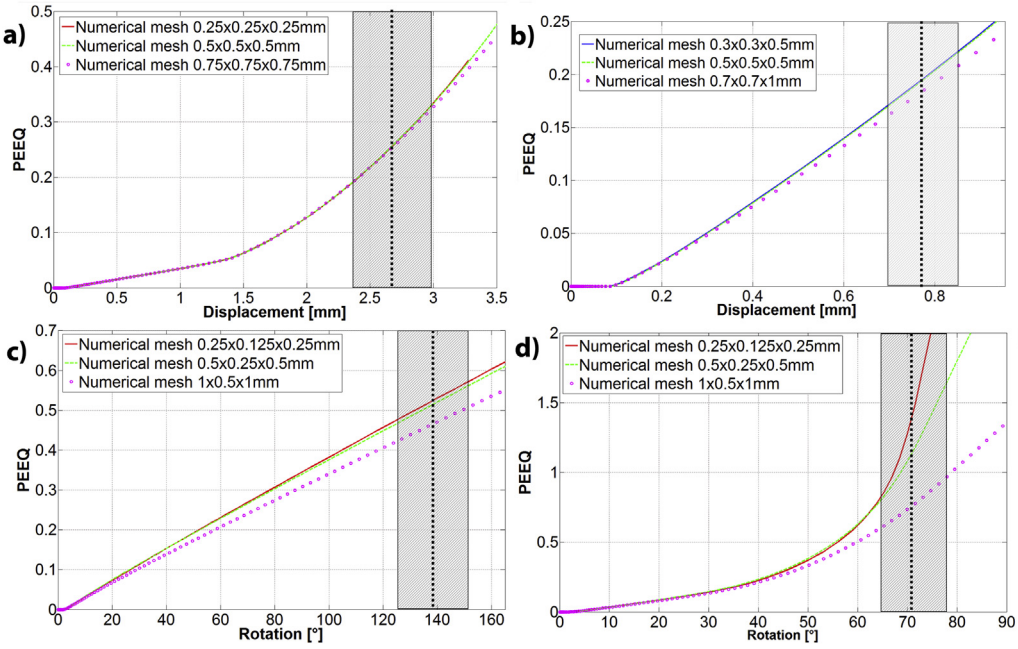

Fig. 3. Effect of the mesh size on the equivalent plastic strain. Experimental fracture happens in the grey hatched area. The vertical black hatched line indicates the point considered for the calibration. a) tensile test on a round smooth specimen, b) tensile test on a round notched specimen (5 mm notch radius), c) pure torsion, d) multi-axial (superimposed tension 4KN).

0 and 0.1) present a very peculiar behaviour. It is clearly visible that there is a sharp modification in the estimation of the plastic strain at failure between the pure torsion (triaxiality equals to 0) and the two multiaxial tension-torsion test. This paper is not aimed at the investigation of this behaviour but it will be the object of future extensive investigations. As far as the other points are concerned, the hyperbola fits the experimental data satisfactorily.

4.3. Calibration of the MMC fracture surface

According with the analysis stated in Paragraph 2.2.2, the MMC takes into account not only the stress triaxiality, but also the Lode angle dependency. Thus, the fracture locus is no longer a curve, as for the BW model, but it is rather a surface (in the space of triaxiality and Lode angle). Starting from the experimental⧹numerical

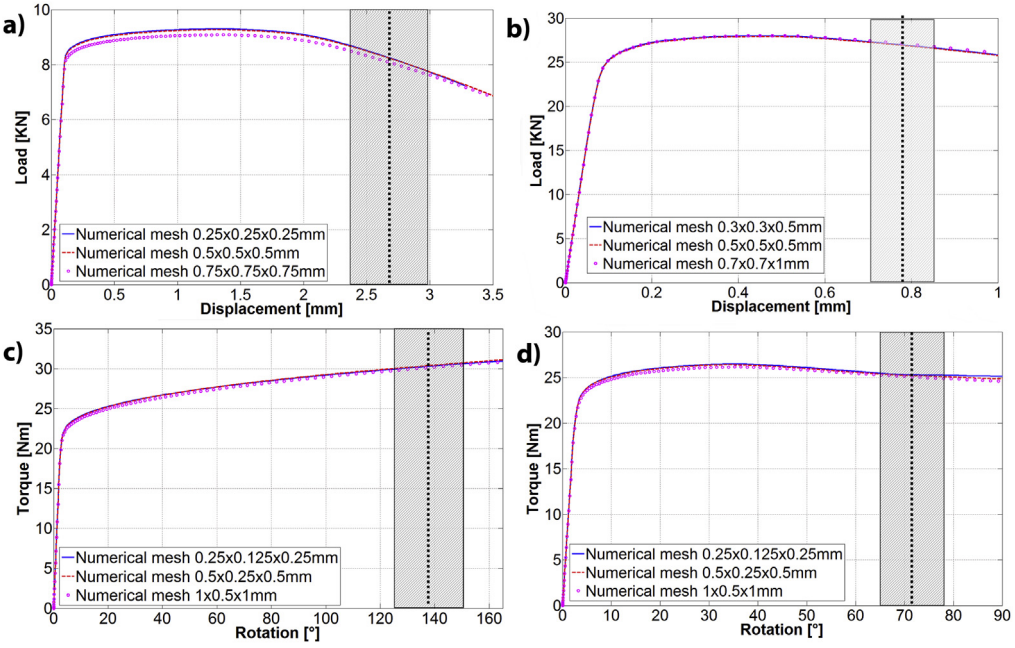

Fig. 4. Effect of the mesh size on the load/displacement curves. Experimental fracture happens in the grey hatched area. The vertical black hatched line indicates the point considered for the calibration. a) tensile test on a round smooth specimen, b) tensile test on a round notched specimen (5 mm notch radius), c) pure torsion, d) multi-axial (superimposed tension 4KN).

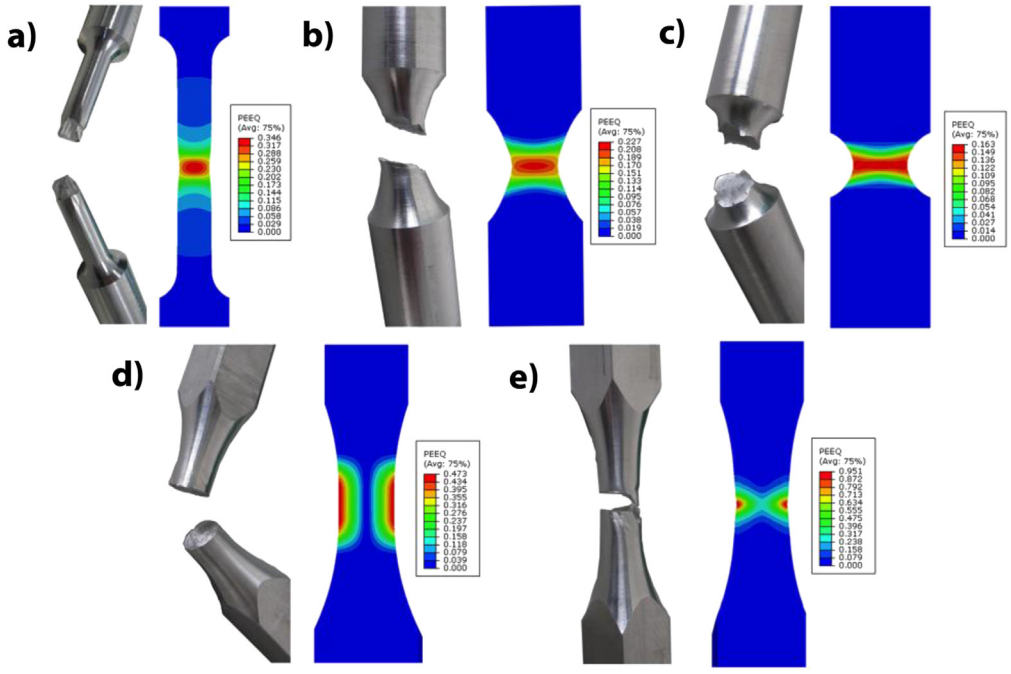

Fig. 5. Virtual test and experimental specimen at the end of the test. Colours represent the value of the equivalent plastic strain PEEQ. a) Round smooth, b) round notched (notch radius 12 mm), c) round notched (notch radius 5 mm), d) pure torsion test, e) multi-axial (superimposed tension 4KN). (For interpretation of the references to colour in this figure legend, the reader is referred to the web version of this article.)

Table 4
Definition of the new fracture locus calibrated for Al 6061-T6.

Equation	Calibrated parameters	
$\varepsilon_f = \frac{k_1}{\frac{1}{3}+\eta} + k_2$	k_1	k_2
	0.2436	*0.04389*

data described in the previous paragraph, it is possible to determine the MMC fracture surface. This requires the evaluation of the Lode angle parameter history and its elaboration in the same way as for triaxiality. These data can be obtained by means of Eq. (5). Fig. 7 shows the Lode angle history for each simulated test and its final average value.

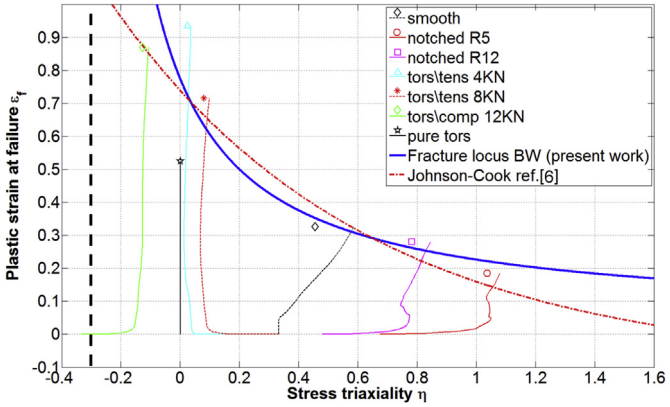

Fig. 6. Calibrated fracture locus along with plastic strain vs. stress triaxiality history until failure. Average representative points for each test are presented (average stress triaxiality, η_{av}, equivalent plastic strain at the onset of the failure, ε_f). A literature Johnson–Cook fracture locus is also reported.

In order to determine the final MMC criterion five different constants have to be determined. Two of them (A, n) are parameters of the plasticity hardening law defined by Eq. (10)

$$\sigma = A_{PL}(\varepsilon_p)^{n_{PL}} \tag{10}$$

Then, using a Matlab subroutine, the experimental points can be fitted to obtain the three remaining free parameters C_1, C_2, C_3. Following Luo [37], the fracture surface has not been fitted using just the average fracture values of triaxiality and Lode angle but, the complete load history has been taken into account. This approach is summarized in Eq. (11)

$$\text{Min}(\text{Error}) = \text{Min}\left[\frac{1}{N}\left(1 - \sum_{i=1}^{N}\int_0^{\bar{\varepsilon}_f}\frac{d\varepsilon_p}{\varepsilon_f}\right)^2\right] \tag{11}$$

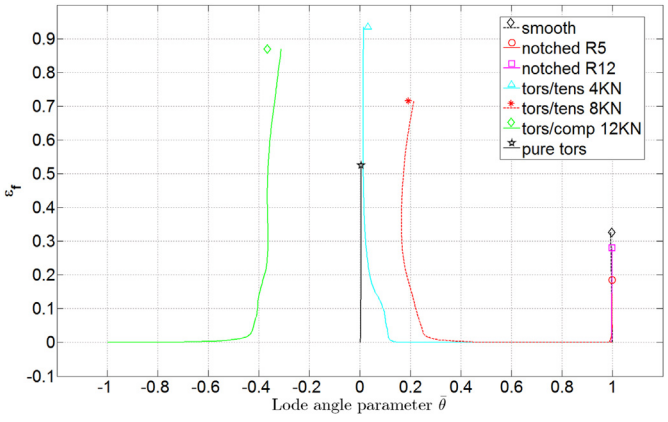

Fig. 7. Lode angle parameter history for each experimental test.

In Fig. 8, the MMC fracture surface is shown. The filled black circles represent the average fracture point with a superimposed error bar. It is important to underline that the lack of an exact overlap of the fracture surface with the average point is caused by the approach followed to obtain the fracture surface. The average points provide a quick overview of the Lode angle ⧹ triaxiality state at fracture but they do not form the base for the interpolation: the complete load history has been taken into account for the interpolation. Finally, in Table 5 the five MMC parameters are summarized.

For a plane stress load condition a unique relation between triaxiality and Lode angle parameter, Eq. (8), can be determined and thus the strain at failure can be described as a function of only the triaxiality. Fig. 9 shows the comparison between the BW fracture locus and the MMC fracture locus evaluated for a plane stress case. If the MMC criterion is applied in a plane stress load scenario, not the entire fracture surface is involved but only the curve described in Fig. 9 is considered. The BW and the plane stress projection of the MMC criterion show a satisfactory agreement over a wide triaxi-ality range but in some regions, the differences are not negligible; what makes the application of the BW criterion reasonable, in case of the simulation of the ballistic impact, is not only the thin walled structure but also a peculiarity of the phenomenon under investi-gation. During the ballistic impact, the stress triaxiality of the cy-lindrical target oscillates largely (see Fig. 17) hence there is no a relatively constant state of stress despite what happens during the calibration tests, or in the other validation applications. The consequence is that the error is not high as it could be in case the two fracture locus would be applied to describe a phenomenon having an almost constant triaxiality and belonging to the regions where the differences are the highest. Practically the large oscilla-tions of the target triaxiality lead to a reduction of the differences applying the two curves (BW and the plain stress projection of the MMC) and eventually lead to the possibility to apply in this case a BW approach neglecting Lode angle effects (hyperbola fit and not a three branches curve) but expecting a limited variation of the result. Moreover, in ballistic impact simulation the most important parameter is the cut-off values for the negative stress triaxiality. Without the cut-off, there will be a physically unrealistic removal of elements at the interface between the projectile and target. Those elements see large compressive stresses under which no fracture should occur. This problem was extensively studied by Teng &Wierzbicki (2006) [17], who showed that the JC failure envelope

Table 5
MMC parameters for Al6061-T6.

MMC parameters
A_{PL} 423.8 MPa
n_{PL} 0.07508
C_1 0.089
C_2 225.11 MPa
C_3 0.928 MPa

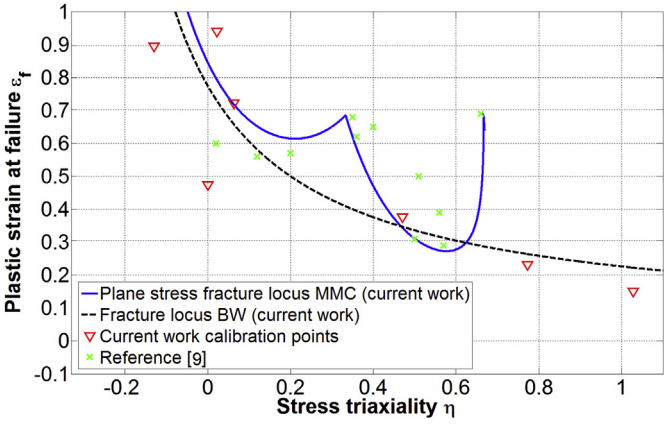

Fig. 9. Comparison between the BW fracture locus calibrated in the present research with the plane stress fracture locus (MMC).

without the cut-off property resulted in very unrealistic pattern during projectile penetration.

It is interesting to compare the data obtained in the present research with the data obtained on the same Al 6061-T6 aluminium in Ref. [9]. The data are slightly different because the different state of the original material from which the specimen have been cut: in the actual research it is bulk whereas in Ref. [9] specimen were obtained from sheets. However, comparing the plane stress fracture locus curve obtained in Ref. [9], the similarity of the points obtained for the plane stress with the present research is evident, Fig. 9.

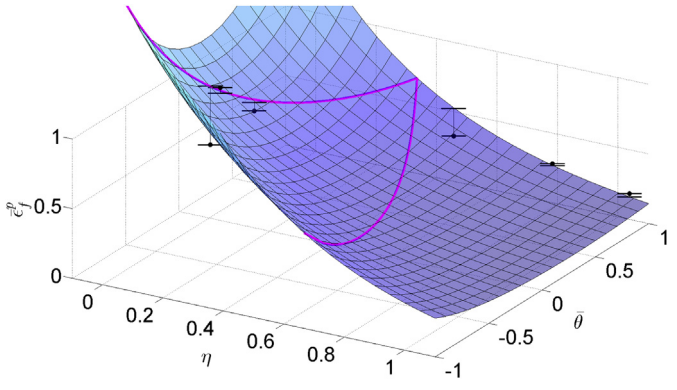

Fig. 8. MMC fracture surface. Black circles are the average final values. The solid lines represent the difference between the fracture surface and the average points. The red line over the surface represents the plane stress condition. (For interpretation of the references to colour in this figure legend, the reader is referred to the web version of this article.)

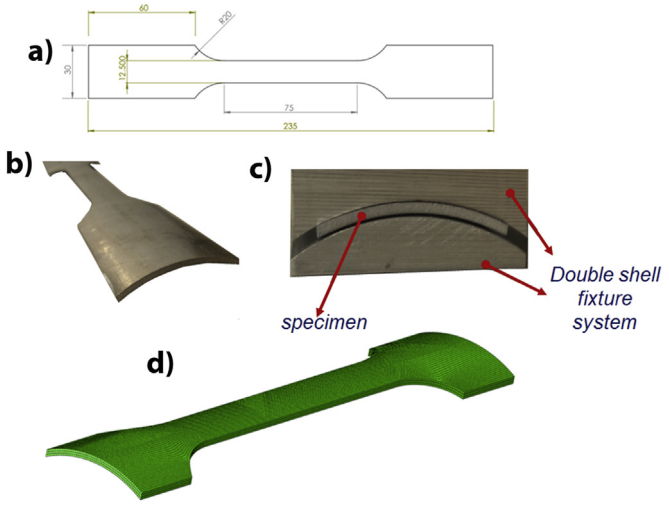

Fig. 10. a) Technical drawing of the specimen cut from the tube b) view of the specimen c) details of the fixture system d) numerical model.

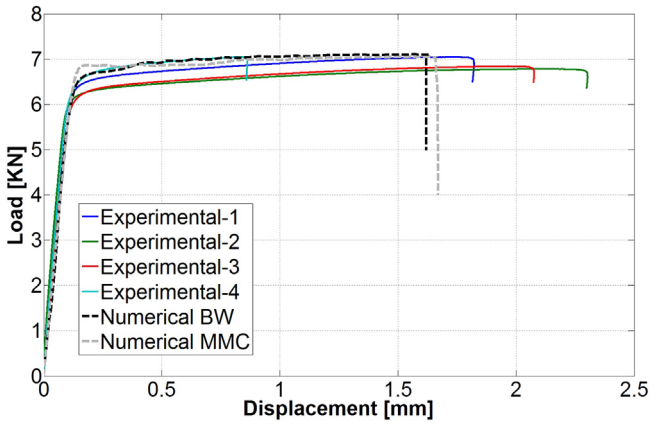

Fig. 11. Comparison between experimental and numerical results for the tensile test of specimen cut directly from a thin walled tube (transmission shaft).

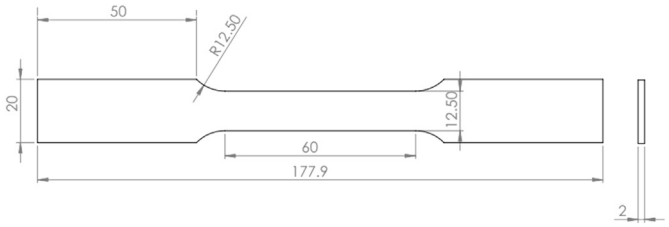

Fig. 12. Technical drawing of a flat dog-bone specimen.

5. Validation of the constitutive law and the fracture locus on components having a different machining history

5.1. Specimens cut directly from a tubular shaft

An assessment of the goodness of material calibration has been carried out on a tubular shaft representing a component of the tail rotor transmission of a helicopter.

The tubular shaft has an outer diameter of 63.5 mm and a wall thickness of 1.65 mm. It is therefore not feasible to obtain round specimens, which allow to carry out all the required tests.. Thus, only a tensile test on a specimen directly cut from the thin walled tube has been carried out. . Subsequently, it has been numerically reproduced adopting the material calibration found previously

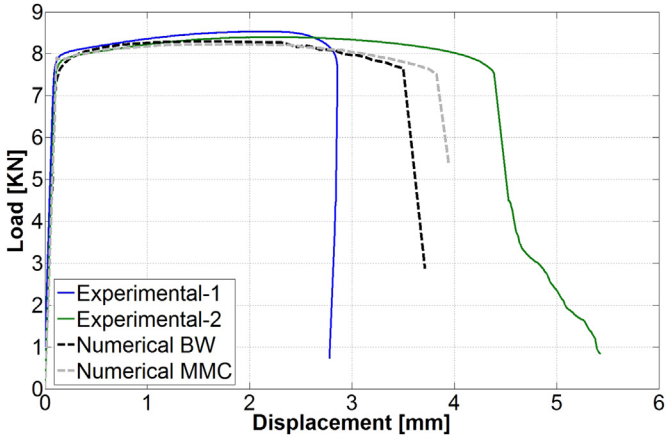

Fig. 13. Comparison between experimental and numerical results for the tensile test of flat dog-bone specimen.

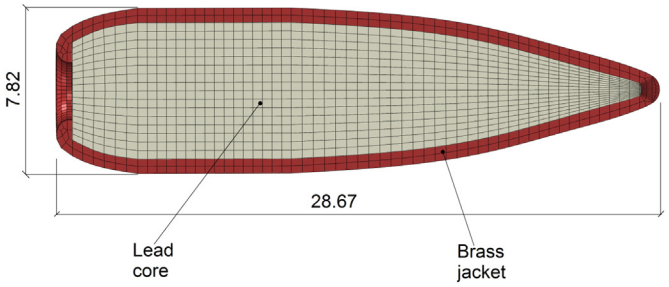

Fig. 14. Longitudinal section of the 7.62 × 51 ball bullet.

(both MMC and BW models have been applied). A water jet cutting technique has been used to cut specimens from the tested tube, leaving a residual curvature, due to the radius of the original tube, in the specimen. This lead to the development of a special fixture system in order to allow tests on a standard MTS machine. The main goal of the fixture is to provide a flat surface for the machine grips but at the same time to avoid the application of an eccentric load. The fixtures consist of a pair of aluminium shells-like clamps with one rounded face (with the same radius of the internal and external specimen) and one flat face, as shown in Fig. 10b–c). The shape of the fixtures has been optimized to guarantee the coaxiality between the load axis and the barycentric specimen axis. In Fig. 10a) a drawing of the specimen is shown. This shape is the projection of the real specimen on a flat plane. The waterjet cut may create a not perfect free edge and this may be responsible for the some scatter of the experimental results. Besides, it is possible that some minor slides happen between the specimen and the grips thus increasing the variability of the results.

A numerical model able to reproduce the experimental tests was developed following the same approach described for the other numerical tests explained in the paper. For this purpose, an Explicit solver (ABAQUS) with a quasi-static approach and solid elements C3D8R has been adopted. The model consists of 31596 elements with an average size of 0.5 × 0.449 × 0.578 mm. The strain rate and the thermal dependence on plasticity have not been considered in the simulations. Fig. 11 compares the experimental and numerical results. The calibration of the material reproduces with a reasonable accuracy the plastic behaviour of the specimens and satisfactorily estimates fracture. Both the BW and the MMC fracture criterion were applied. The results concerning the prediction of displacement at failure show similarity between the two models. Differences in the plateau region of the two numerical analyses are due to a slight difference in the constitutive law used for the BW and MMC. According with the original derivation of the MMC criterion, the plasticity model to be adopted is a power law and therefore, in order to remain consistent with MMC formulation a power law has been used along with MMC. The power law is not a perfect approximation to the reference exponential JC hardening law, which has been adopted for all the calibrations. Discrepancies in the FE results, between BW and MMC, are also due to the minor differences related with the procedure adopted to get the power law parameters starting from the JC ones.

5.2. Flat specimen

Uniaxial tensile tests of specimen cut from bulk material offer further evidence on the accuracy of the material calibration, specifically those specimens have been obtained from the same virgin material used for the calibration. Numerical models of the experimental tests show good similarity with not only the experimental load/displacement curves, but also regarding their estimation of

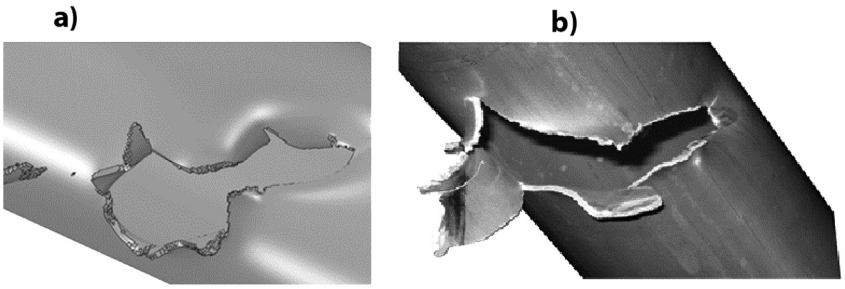

Fig. 15. Comparison of the numerical a) and the experimental damage b).

the displacement at failure. These results further demonstrate that the actual constitutive law, with the BW or MMC fracture model, is satisfactorily able to reproduce also a plane stress scenario. Fig. 12 shows the technical drawing of the dog-bone specimen and in Fig. 13 the numerical and experimental load/displacement curves are compared. Explicit solver (ABAQUS) with a quasi-static approach and solid elements C3D8R has been adopted. The model consists of 12,000 elements with a size in the fracture region of 0.5 × 0.5 × 0.48 mm. The strain rate and the thermal softening effect on plasticity have not been considered in these simulations.

6. Application of the fracture model in a high velocity impact: ballistic impact of a 7.62 ogival soft core bullet against a transmission shaft

An experimental programme on high velocity impact, along with some preliminary analyses, was carried out by the authors [38,39]. A very simplified numerical modelling approach was previously presented in Ref. [38] whereas a similar (to the present paper) approach was applied in Ref. [39] to study the ballistic damage. The present paper uses a slightly different approach for the BW criterion and an improved calibration of the bullet material as illustrated hereafter. Moreover, the current work is aimed more specifically at the assessment of the transferability and the validation of the calibrated mechanical properties, whereas in Refs. [38,39] the focus lies on the experimental tests on the shaft and on the development of a damage tolerant approach.

The problem was modelled in ABAQUS, adopting its Explicit solver. The impact zone mesh of the shaft is refined, having 4 ele-ments through the wall thickness with a dimension of 0.5 × 0.5 × 0.41 mm^3. The adopted elements are solid with a reduced integration C3D8R with an enhanced hourglass control. The projectile is a 7.62 × 51 mm ball bullet (ogival tip). It is a full metal jacket bullet, with a brass coating (Young modulus 115,000 MPa, Poisson coefficient 0.31 [5]) and an alloyed lead core (Young modulus 16,000 MPa, Poisson coefficient 0.42 [5]). The bullet is considered completely deformable and modelled by means of a specific constitutive law and a ductile damage criteria for both the two components of the assembly (core and jacket), Fig. 14.

The velocity of the projectile impact from small arms of 850 m/s produces strain rates of an order of $10^4\ s^{-1}$. As described previously in the paper, the effect of strain rate sensitivity must be taken into account. Concerning the shaft, the strain rate and temperature dependent JC model was used, adopting the parameters reported in Table 6. The temperature dependence parameter has been found in Ref. [6] and the strain rate dependence parameter has been found in Ref. [5]. In addition, the thermo-mechanical coupling is considered with the Taylor−Quinney coefficient of 0.9.

For what concerns the bullet (core and jacket), a JC plasticity model with strain rate and temperature dependence along with a constant fracture damage criterion has been chosen. Data are derived from a specific experimental programme based on specimens made directly from lead and brass alloy of core and jacket [7,8]. These data were evaluated from specimen obtained prior to the final manufacturing of the bullet.

The bullet calibration parameters are reported in Table 7. The projectile has been modelled as a deformable body and reduce integration brick elements have been used. The core is composed of 12488 elements with an average dimension of 0.27 mm whilst the jacket has 6929 elements with an average dimension of 0.26 mm.

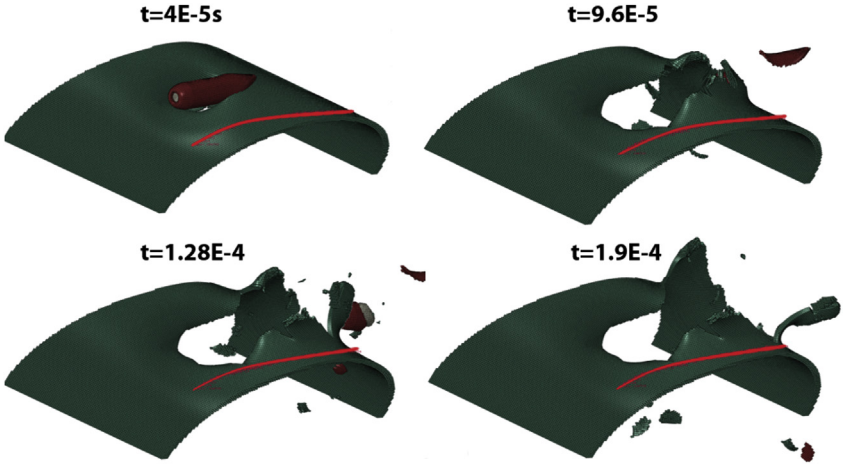

Fig. 16. Different stages of the perforation process. The red path highlighted is the undamaged path. (For interpretation of the references to colour in this figure legend, the reader is referred to the web version of this article.)

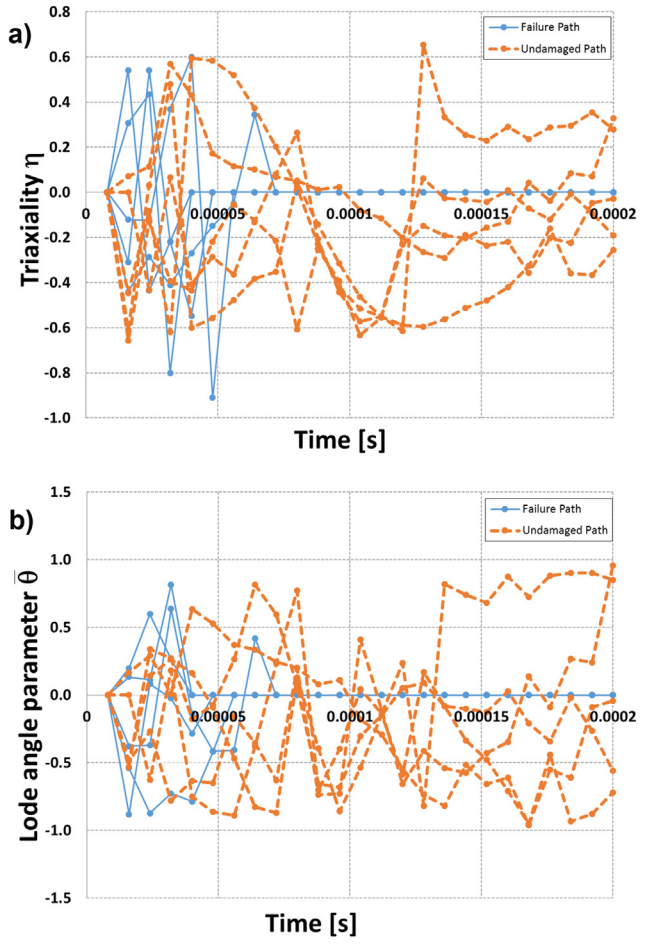

Fig. 17. Triaxiality a) and Lode angle parameter b) evaluated for two series of elements along the failure path and along the undamaged path as highlighted in Fig. 16.

Table 6
Aluminium Al6061: Constants for the JC model (strain rate and temperature dependency) [6,5].

$\dot{\varepsilon}_0[s^{-1}]$	597.2
C	0.1301
m	1.34
T_f [K]	925

The friction between the projectile and the shaft was neglected. An oblique 45° oriented impact condition and with a proper offset (with respect to the longitudinal axis of the shaft) is considered in the tests, which, according to Colombo [40], is the most dangerous one. It causes damage in the shaft in the form of a single large hole. The initial translation velocity of the bullet is 845 m/s and the spin velocity around its longitudinal axe is 750 RPM, which correspond to the common real impact conditions for this kind of projectile [40]. The numerical calibration of the material previously illustrated provides excellent results both in terms of residual velocity, 721 m/s (with experimental one of 718 m/s), and in terms of reproducing the real damage shape. Also a refined mesh of 0.25 × 0.25 × 0.25 mm has been tested and a difference in the predicted residual velocity of 0.5% and a difference in the trajectory of about 4.9% were found, compared with the coarse mesh. On these bases, is reasonable to develop all the following analysis adopting the "coarse" mesh of 0.5 × 0.5 × 0.41 mm because the differences are completely negligible but the simulation is about 2 times faster.

The analyses using the actual calibrated fracture locus show a very realistic damage. The impact involves a wide area of the shaft and the bullet brass jacket is severely damaged allowing the soft lead alloy to impact against the pipe, Figs. 15 and 16. Fig. 15 shows a comparison between the numerical and the experimental damage. The numerical model is able to accurately reproduce the real damage and in particular the petalling phenomena are well reproduced. The numerical simulation points out into the importance of the calibration of a fracture locus over a large range of state of stress. Fig. 17 shows the trend of the Lode angle and the triaxiality for the elements belonging to two different paths: failure path is the one along the same trajectory of the bullet, the undamaged path is a path parallel to the previous one but in which no element deletion takes place along it (see Fig. 16). Data from five different elements for each path have been collected and compared in Fig. 17. Fig. 17 clearly shows the high oscillation of both triaxiality and Lode angle, especially for failed elements. As expected, along the failure path, once elements have been deleted, their triaxiality and Lode angle are correctly set to zero. Their trend before failure is however comparable with the trend of the elements regarded in the un-damaged path. Oscillations are amplified by the impulsive load due to impact and by the thin walled structure of the shaft. Indeed, the ballistic impact can be considered as an impulsive load, which generates relevant displacement oscillations into the target. Moreover, the oscillations are also amplified by the instantaneous deletion of failed elements. At any rate in both paths, the waving behaviour of the stress state inside the elements is complex and this makes its estimation almost impossible prior to running numerical analyses.

6.1. Estimation of the effect of impact on the rotating shaft

The impact tested shaft represents a section of the rear tail transmission of a helicopter hence, for the real working conditions, the impact between the shaft and the bullet happens whilst the shaft is rotating. The possibility to experimentally reproduce such conditions is not easy because it is necessary to design a proper system to put into rotation the shaft and a shield in order to protect from damage this moving system during the test. This is a clear example where a virtual testing methodology could be usefully exploited.

The numerical tests have been performed keeping the previous most critical impact conditions (45° obliquity and offset). The only difference is that the shaft has a constant rotating velocity of 3000 RPM. Results have been analysed on two levels:

- Bullet trajectory modification
- Damage shape of shaft and bullet

Table 7
Projectile properties [7,8].

Part	Constitutive equation	A_{PL} [MPa]	B_{PL} [MPa]	n_{PL}	C	$\dot{\varepsilon}_0[s^{-1}]$	m	T_a [K]	T_f [K]	Fracture locus	Strain at failure ε_f
Core (lead)	JC	0	55.552	0.0987	0.2312	72.108	1	294	525	Constant strain to failure	31%
Jacket (brass)	JC	90	628.03	0.7201	0.2659	745.82	1.68	294	1300	Constant strain to failure	40%

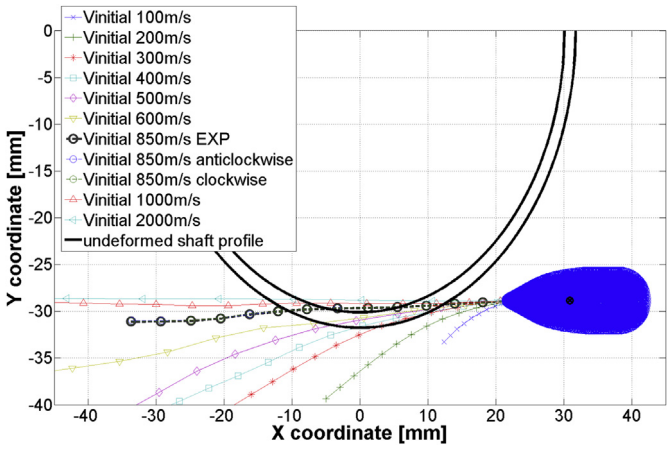

Fig. 18. Trajectory of the bullet as a function of its initial translational velocity.

Several numerical tests have been performed in order to define how the trajectory of the bullet is influenced by the impact velocity while hitting the locked shaft, Fig. 18. In the above-mentioned figure is represented the undeformed section of the shaft, the initial bullet position and the trajectory of its barycentre for different initial velocities. The amount of intersection between the trajectory lines and the undeformed shape of the shaft can be considered as related at the damage suffered by the tube. It is evident that for speed up to 300 m/s there is a heavy richochet phenomenon, so the bullet does not penetrate the shaft and there is a clear rebound effect. For velocities of 400, 500 and 600 m/s the deviation of the trajectory is less evident and the intersection with the profile of the shaft is more evident, showing that the damage of the tube is increasing. For the real experimentally tested velocity, 850 m/s, and for the higher ones (up to 2000 m/s) there is almost no trajectory deviation, so there is a complete penetration of the shaft which is not robust enough to lead a rebound of the bullet. Clock-wise and anticlockwise rotation has been studied; Fig. 18 shows clearly that at a velocity of 850 m/s (the real bullet conditions) there is no effect of the rotation of the shaft on the trajectory. This result is reasonable also considering the velocities involved in the problem. Considering a rotation speed of the shaft of 3000 RPM and its external radius of 31.75 mm, from simple calculations, the maximum tangential velocity is 10 m/s, which is much smaller than the 850 m/s initial translation velocity of the bullet. Hence, it is reasonable to expect that the rotation of the shaft has a barely visible effect on trajectory.

However, it is of interest also the evaluation of the possible effect of the rotation of the shaft in terms of damage shape because it would be possible that even if the trajectory is not affected, the damage shape could potentially change in a non-negligible way. Fig. 19 shows the damage shape of the bullet and the shaft for three different conditions. Fig. 19a shows the results for the fixed configuration, Fig. 19b represents the case where an anticlockwise velocity rotation is applied to the shaft (the tangential velocity of the shaft is opposite to the speed direction of the bullet). Finally, Fig. 19c shows the condition of a clockwise rotational speed applied to the shaft. Again, it is evident that with the tested ratio between impact velocity and rotating velocity of the shaft, there are no relevant differences among the various cases. In Fig. 19d and e, the geometrical initial impact conditions are reported, showing the initial position of both the shaft and the bullet from two different points of view. Fig. 19 shows clearly that even from a morphological point of view the effect of the rotation of the shaft is negligible for both the shaft and the bullet. Both components have very few and small differences in their damage shape comparing the various cases and this is consistent with the previous discussion concerning trajectory modifications and speed of the involved body.

7. Conclusion

The main goal of the paper is to use a dedicated material calibration to estimate an extreme loading condition: the damage of a helicopter tail rotor transmission shaft, made in aluminium Al6061-T6, due to a small arm ballistic impact. In order to do that the paper goes through all the steps from the calibration of a ductile damage criterion (BW and MMC) up to its application for the

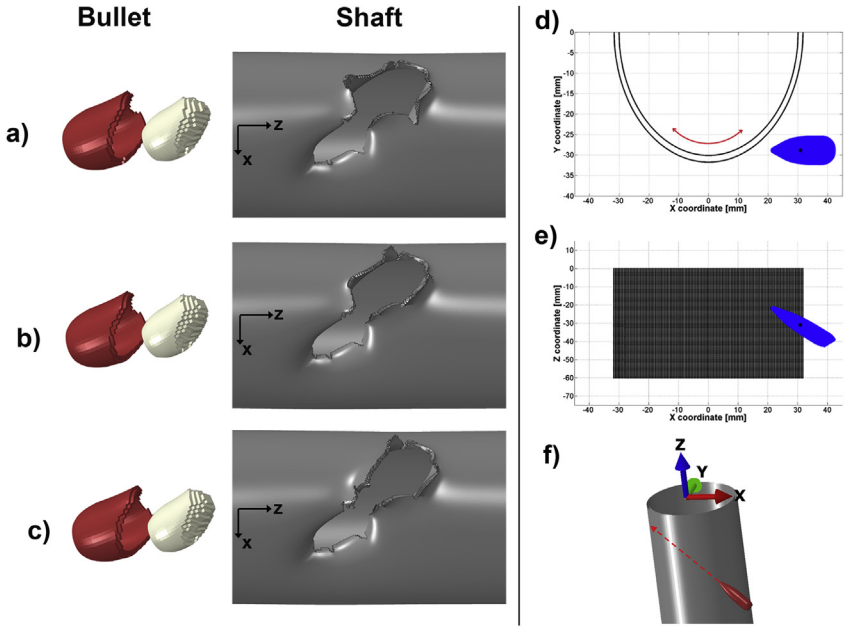

Fig. 19. Evaluation of the final damage shape of bullet and shaft for a) non-rotating shaft b) 3000 RPM anticlockwise rotation of the shaft c) 3000 RPM clockwise rotation of the shaft d–f) visualization of the impact conditions: different views.

simulation of the complex load scenario (ballistic impact). The Al6061-T6 has been characterized by means of a methodology based on quasi-static uniaxial and multiaxial tests at room temperature, along with an inverse calibration method. Compared with the literature, the approach based on the combination of bulk specimen and multiaxial test, allowed to study a very large range of Lode angles and triaxialities. In particular, the low stress triaxiality range ($0 \leq \eta \leq 0.4$) has been investigated, showing the presence of a minimum for pure shear torsional load. This behaviour is not novel but it is still under debate in the literature and the manuscript gives additional data to the scholars. In the calibration stage, the robustness of the numerical models has been evaluated performing mesh size analysis, which demonstrate that the elements size differently affects the tensile test, the torsion and multi axial test. It has been verified that multi axial tests are the most prone to a mesh size effect.

Both the MMC and BW models show good capability to reproduce load conditions not adopted for their calibration (geometry transferability). This capability has been evaluated reproducing the tensile test of dog-bone specimen and the tensile test of a specimen cut directly from a shaft (the same used for ballistic impact). This latter test is very important because it highlights the possibility to adopt a model calibrated from specimen cut from bulk material to reproduce the behaviour of specimen made of material having the same nominal chemical composition and heat treatment, but obtained through a different manufacturing process.

Furthermore, the BW criterion has been chosen to simulate the ballistic impact simulation of 7.62 ball bullet against an Al6061-T6 aluminium shaft. The comparisons between experiments and numerical results show a good correlation concerning both the damage shape and the residual velocity of the bullet.

Finally, once having established confidence in the numerical simulation, the FE model of the ballistic impact has been exploited adopting a purely virtual testing approach, investigating a scenario where experimental evidences are not available. Specifically, the effect of a superimposed rotational velocity of the shaft during the impact was studied. It was found that with the imposed velocities of the bullet (850 m/s), the shaft rotation (3000 RPM) does not affect the projectile trajectory and neither the damage shape of bullet and shaft itself.

Acknowledgement

The authors would like to thank the program Progetto Rocca for the financial support received for the research carried out at MIT by A. Gilioli as a visiting student.

References

[1] Bao Y, Wierzbicki T. A comparative study on various ductile crack formation criteria. J Eng Mater Technol 2004;126(3):314–24.
[2] Li H, Fu MW, Lu J, Yang H. Ductile fracture: experiments and computations. Int J Plast 2011;27:147–80.
[3] Bao Y, Wierzbicki T. Bridgman revisited, on the history effects on ductile fracture. 2004. Technical Reports No. 112 of the Impact and Crashworthiness Lab, Massachusetts Institute of Technology, 77 Massachusetts Ave, Cambridge, MA 02139, United States.
[4] Johnson GR, Cook WH. Fracture characteristics of three metals subjected to various strains, strain rates, temperatures and pressures. Eng Fract Mech 1985;21:31–48.
[5] Manes A, Peroni L, Scapin M, Giglio M. Analysis of strain rate behavior of an Al 6061 T6 alloy. Procedia Eng 2011;10:3477–82.
[6] Lesuer DR, Kay GJ, LeBlanc MM. Modeling large-strain, high rate deformation in metals. Livermore, CA 94550, United States of America: Lawrence Livermore National Laboratory; 2001. UCRL-JC-134118.
[7] Peroni L, Scapin M, Fichera C, Manes A, Giglio M. Mechanical properties at high strainrate of lead core and brass jacket of a NATO 7.62 mm ball bullet, proceedings of DYMAT 2012. In: 10th International Conference on the Mechanical and Physical Behaviour of Materials under Dynamic Loading, Freiburg, Germany, EPJ Web of Conferences, vol. 26, 01060. EDP Sciences; 2012. http://dx.doi.org/10.1051/epjconf/20122601060.
[8] Giglio M, Gilioli A, Manes A, Peroni L, Scapin M. Investigation about the influence of the mechanical properties of lead core and brass jacket of a NATO 7.62 mm ball bullet in numerical simulations of ballistic impacts, Dymat. In: 10th International Conference on the Mechanical and Physical Behaviour of Materials under Dynamic Loading, Freiburg, Germany, EPJ Web of Conferences, vol. 26, 04010. EDP Sciences; 2012. http://dx.doi.org/10.1051/epjconf/20122604010.
[9] Beese AM, Luo M, Li Y, Bai Y, Wierzbicki T. Partially coupled anisotropic fracture model for aluminum sheets. Eng Frac Mech 2010;77:1128–52.
[10] Viganò F, Manes A, Giglio M. Ductile fracture locus of Ti-6Al-4V titanium alloy. Int J Mech Sci 2012;54:121–35.
[11] Papasidero J, Doquet V, Mohr D. Determination of the effect of stress state on the onset of ductile fracture through tension-torsion experiments. Exp Mech 2013. http://dx.doi.org/10.1007/s11340-013-9788-4.
[12] Cockcroft MG, Latham DJ. Ductility and the workability of metals. J Inst Metals 1968;96:33–9.
[13] Børvik T, Hopperstad OS, Pedersen KO. Quasi-brittle fracture during structural impact of AA7075-T651 aluminium plates. Int J Impact Eng 2010;37:537–51.
[14] Børvik T, Dey S, Clausen AH. Perforation resistance of five different high-strength steel plates subjected to small-arms projectiles. Int J Impact Eng 2009;36:948–64.
[15] Bai Y, Wierzbicki T. Application of extended Mohr–Coulomb criterion to ductile fracture. Int J Fract 2010;161:1–20.
[16] Teng X, Wierzbicki T, Huang M. Ballistic resistance of double-layered armor plates. Int J Imp Eng 2008;35(8):870–84.
[17] Teng X, Wierzbicki T. Evaluation of six fracture models in high velocity perforation. Eng Fract Mech 2006;73(12):1653–78.
[18] Dabboussi W, Nemes JA. Modeling of ductile fracture using the dynamic punch test. Int J Mech Sci 2005;47:1282–99.
[19] Zukas JA, Nicholas T, Swift HF. Impact dynamics. New York: Wiley; 1982.
[20] Clausing DP. Effect of plastic strain state on ductility and toughness. Int J Fract Mech 1970;6:71–85.
[21] McClintock FA. Plasticity aspects of fracture. In: Liebowitz H, editor. Fracture. New York: Academic Press; 1971.
[22] Viganò F, Manes A, Giglio M. Numerical simulation of the slant fracture of a helicopter's rotor hub with a ductile damage failure criteria. Fatigue Fract Eng M 2012;35(4):317–27.
[23] Chiantoni G, Bonora N, Ruggero A. Experimental study of the effect of triaxiality ratio on the formability limit diagram and ductile damage evolution in steel and high purity copper. Int J Mater Form 2010;3(1):171–4.
[24] Barsoum I, Faleskog J. Rupture mechanisms in combined tension and shear experiments. Int J Solids Struct 2007;44(6):1768–86.
[25] Korkolis YP, Kyriakides S. Inflation and burst of anisotropic aluminum tubes for hydroforming applications. Int J Plast 2008;24(3):509–43.
[26] Zhao J. Applicability of Mohr-Coulomb and Hoek-Brown strength criteria to the dynamic strength of brittle rock. Int J Rock Mech Min Sci 2000;37(7):1115–21.
[27] Palchik V. Application of Mohr-Coulomb failure theory to very porous sandy shales. Int J Rock Mech Min Sci 2006;43(7):1153–62.
[28] Bai Y, Wierzbicki T. A new model of metal plasticity and fracture with pressure and lode dependence. Int J Plast 2008;24(6):1071–96.
[29] Bai Y. Effect of loading history on necking and fracture. MIT PhD thesis. 77 Massachusetts Ave, Cambridge, MA 02139, United States: Massachusetts Institute of Technology; 2008.
[30] Bao Y, Wierzbicki T. On fracture locus in the equivalent strain and stress triaxiality space. Int J Mech Sci 2004;46:81–98.
[31] Xue L. Damage accumulation and fracture initiation in uncracked ductile solids subject to triaxial loading. Int J Solids Struct 2007;44(16):5163–81.
[32] Roth CC, Mohr D. Effect of strain rate on ductile fracture initiation in advanced high strength steel sheets: experiments and modelling. Int J Plast 2014;56:19–44.
[33] www.matweb.com.
[34] Manes A, Pagani M, Saponara M, Mombelli D, Mapelli C, Giglio M. Metallographic characterisation of Al6061-T6 aluminium plates subjected to ballistic impact. Mater Sci Eng A 2014;608:207–20.
[35] Driemeier L, Brunig M, Micheli G, Alves M. Experiments on stress-triaxiality dependence of material behavior of aluminum alloys. Mech Mater 2010;42:207–17.
[36] Bao Y, Wierzbicki T. On the cut-off value of negative stress triaxiality for fracture. Eng Fract Mech 2005;72:1049–69.
[37] Luo M. Anisotropic ductile fracture of metal sheets: experimental investigation and constitutive modelling. MIT PhD thesis. 77 Massachusetts Ave, Cambridge, MA 02139, United States: Massachusetts Institute of Technology; 2012.
[38] Giglio M, Manes A. Terminal ballistic effect on the crack growth assessment of a helicopter rotor drive. Eng Fract Mech 2011;78(8):1542–54.
[39] Manes A, Lumassi D, Giudici L, Giglio M. An experimental-numerical investigation on aluminium tubes subjected to ballistic impact with soft core 7.62 ball projectiles. Thin Wall Struct 2013;73:68–80.
[40] Colombo D, Giglio M. Numerical analysis of thin-walled shaft perforation by projectile. Comput Struct 2007;85:1264–80. Elsevier Applied Science.